Eddy-Induced Salinity Changes in the Tropical Pacific

Thierry Delcroix, Alexis Chaigneau, D. Soviadan, Jacqueline Boutin, Cori Pegliasco

JGR Oceans

RESEARCH ARTICLE
10.1029/2018JC014394

Eddy-Induced Salinity Changes in the Tropical Pacific

T. Delcroix[1], A. Chaigneau[1,2,3], D. Soviadan[3], J. Boutin[4], and Cori Pegliasco[1]

[1]LEGOS, CNES, CNRS, IRD, UPS, University of Toulouse, Toulouse, France, [2]Institut de Recherches Halieutiques et Océanologiques du Bénin, Cotonou, Benin, [3]International Chair in Mathematical Physics and Applications (UNESCO Chair), University of Abomey-Calavi, Cotonou, Benin, [4]Sorbonne Université, CNRS, IRD, MNHN, LOCEAN, Paris, France

Key Points:
- Tropical Pacific SSS mesoscale variability accounts for 40% to 60% of the SSS total variability
- Composites of eddy-induced SSS anomalies reveal a dipole (monopole) pattern in the central (eastern) part of the tropical North Pacific
- The two mechanisms explaining dipole versus monopole eddy patterns likely involve horizontal advection and vertical processes, respectively

Correspondence to:
T. Delcroix,
thierry.delcroix@legos.obs-mip.fr

Citation:
Delcroix, T., Chaigneau, A., Soviadan, D., Boutin, J., & Pegliasco, C. (2019). Eddy-induced salinity changes in the tropical Pacific. *Journal of Geophysical Research: Oceans*, *124*, 374–389. https://doi.org/10.1029/2018JC014394

Received 20 JUL 2018
Accepted 26 DEC 2018
Accepted article online 28 DEC 2018
Published online 17 JAN 2019

Abstract The signature of westward propagating mesoscale eddies in sea surface salinity (SSS) is analyzed for the tropical Pacific by collocating 7 years (2010–2016) of Soil Moisture and Ocean Salinity SSS satellite data with coherent mesoscale eddies automatically identified and tracked from altimetry-derived sea level anomalies. First, the main characteristics of the long-lived coherent eddies are inferred from sea level anomalies maps. Then, the mean signature of the mesoscale eddies on SSS is depicted for the whole tropical Pacific before focusing in regions centered around the central and eastern parts of the tropical North Pacific. In these areas, composite analyses based on thousands of eddies reveal regionally dependent eddy impacts with opposite SSS anomalies for cyclonic and anticyclonic eddies. In the central region, where the largest meridional SSS large-scale gradients and smallest eddy amplitudes are observed, results show dipole-like SSS changes with maximum anomalies on the leading edge of the composite eddy. In contrast, in the eastern region, where the largest near-surface vertical salinity gradients and largest eddy amplitudes are observed, the composite eddy shows monopole-like SSS changes with maximum anomalies near the composite eddy center. These distinct dipole/monopole SSS patterns suggest the dominant role of horizontal advection and vertical processes in the central and eastern regions, respectively. Other possible explanations, notably one involving the contrasted eddy amplitudes of the two regions, are discussed.

Plain Language Summary Sea surface salinity (SSS) is an Essential Climate Variable needed to improve our knowledge of the Earth's water cycle and climate. SSS has proven to be valuable for improving estimates of evaporation minus precipitation ($E - P$) budgets, describing and understanding climate variability at seasonal to decadal time scales, testing physical processes, assessing numerical model skills, quantifying the role of salinity on sea level change, improving El Nino prediction lead time, and quantifying the ocean-atmosphere CO_2 exchanges. Very few studies have, however, focused on what we call small-scale (that is mainly eddies of the order of 50- to 300-km radius) SSS changes in the open ocean, mainly due to the lack of high-resolution measurements. Relying on unprecedented satellite measurements of SSS, the present study shows how eddies in the tropical Pacific can modify the spatial distribution of SSS. We suggest that these modifications are likely due (i) to the rotational sense of the eddies, which move SSS horizontally, and (ii) to their capability to move or mix waters up and down while rotating.

1. Introduction

Changes in the oceans occur over a broad range of time and space scales. Among those scales, the mesoscale includes energetic features having typical spatial scales of tens to several hundreds of kilometers and time scales ranging from a few days to several months. Although previously intuited, the importance of mesoscale variability for the ocean dynamics was pioneeringly revealed from in situ measurements in the North Atlantic Ocean during the 1970s (Mode Group, 1978). This importance was intensely highlighted in the following decades in all ocean basins after the advent of satellite altimetry measurements such as GEOSAT, ERS, and TOPEX/Poseidon (Le Traon et al., 1990; Stammer, 1997). Nowadays, there is no doubt mesoscale variability needs to be considered to properly document and understand the full oceanic variability (Fu et al., 2010; Le Traon & Morrow, 2001).

Mesoscale eddies constitute the main physical process accounting for mesoscale variability, together with current jets and meanders, fronts, and filaments. Based on remote sensing observations, the impact of mesoscale eddies has been identified on various oceanic and atmospheric variables, such as sea surface temperature (SST), sea surface height (SSH), chlorophyll-a concentration (Chl), and surface winds (Chelton et al., 2007; Chelton, Gaube, et al., 2011; Dufois et al., 2014; Stumpf & Legeckis, 1977). Mesoscale eddies were also

documented using eddy-resolving numerical simulations (e.g., see Ubelmann & Fu, 2011, and the references therein). Mesoscale eddies are known to propagate mainly westward due to the beta effect, roughly at the Rossby wave phase speed depending on latitude (Cushman-Roisin et al., 1990), although trajectories of anticyclonic (ACE) and cyclonic (CE) eddies slightly deflect equatorward and poleward, respectively (Chaigneau et al., 2008; Cushman-Roisin et al., 1990; Morrow et al., 2004). At midlatitudes, eddies have mean radii and SSH amplitudes of the order of 50 to 200 km and 5 to 15 cm, respectively (Chelton, Schlax, & Samelson, 2011). They account for as much as 50% of the global SSH variability and, due to their nonlinear character, can trap and transport mass, heat, salt, nutrients, and biological constituents (Chelton, Schlax, & Samelson, 2011; Wunsch, 1999). Eddy horizontal transport occurs in two different ways: over long distances, trapping fluid into their cores while moving westward, and over shorter distances, displacing fluid around their periphery while rotating (the latter to be further discussed). They can also interact with the atmosphere modifying winds, cloud cover, heat fluxes, and precipitations (Frenger et al., 2013; Ma et al., 2016; Villas Bôas et al., 2015). For readers interested in more details, two recent overviews of the main findings about mesoscale eddies can be found in Chelton, Schlax, and Samelson (2011) and McGillicuddy (2016).

Despite the importance of sea surface salinity (SSS) for the global oceanic thermohaline circulation, ocean and atmosphere interactions, and, generally speaking, for climate studies (e.g., Lagerloef et al., 2010), our knowledge of the SSS mesoscale variability remains very limited, mostly due to the small number of high-resolution measurements. To the best of our knowledge, only few observational studies have investigated SSS mesoscale variability and most of them were based on high-resolution (1 to 2 km) thermosalinograph SSS measurements collected from Volunteer Observing Ships (Alory et al., 2015). For instance, measurements along main ship routes in the tropics show that the spatial SSS standard deviation (used to quantify spatial variability) can reach as much as 0.4 over 100 to 200 km, which is the same order of magnitude as the mean regional seasonal cycle amplitudes (Boutin et al., 2016; Delcroix et al., 2005). Note that salinity computations are based on the practical salinity scale (pss-1978), with no units (see Millero, 1993, and recommendations of United Nations Educational, Scientific and Cultural Organization, 1985). Similar values were found when analyzing high-resolution SSS derived from numerical eddy-resolving simulations, for instance, in the global ocean (Vinogradova & Ponte, 2013) or in the Atlantic Ocean (Sena Martins et al., 2015). Focusing on the Coral Sea in the Southwest Pacific, Maes et al. (2013) further showed that a large part of the mesoscale SSS variability in that area can be attributed to mesoscale eddies.

Our recent ability to document SSS from satellites, providing global coverage in less than 8 days at ~50- to 150-km resolution, allows us to enrich our knowledge of SSS mesoscale variability. Notable in this regard are the key contributions of the SSS data sets issued from the Soil Moisture and Ocean Salinity (SMOS; 2010 and ongoing), Aquarius (2011–2015), and Soil Moisture Active Passive (2015 and ongoing) satellite missions (Kerr et al., 2010; Lagerloef et al., 2008; Reul et al., 2013; Tang et al., 2017). Based on these satellite data sets, the signature of mesoscale variability and eddies on SSS has been documented in various regions, in particular, in the North Atlantic subtropical gyre, in the Gulf Stream region, in the Gulf of Mexico, in the Bay of Bengal, in the southern Indian Ocean, and in line with the occurrence of tropical instability waves in the Atlantic and Pacific Oceans (Fournier et al., 2016, 2017; Kolodziejczyk et al., 2015; Lee et al., 2012, 2014; Melnichenko et al., 2017; Reul et al., 2014; Yin et al., 2014). Despite these few studies, little is known about the eddy-induced SSS changes, especially in tropical regions where the influence of mesoscale eddies on SSS remain poorly documented in the literature compared to the influence of the large-scale circulation, climate modes, and long-term trends. Hence, as a complement to these earlier studies, the goal of this paper is to assess how eddies detected from satellite altimetry during the 2010–2016 time period impact the concomitant SSS field inferred from SMOS satellite mission. The emphasis is put on two regions of relatively intense eddy activity and large SSS meridional or vertical gradient in the tropical Pacific Ocean. The study is complemented in these two regions with a quantification of the eddy signatures on the vertical salinity distribution (0–500 m) inferred from Argo floats.

2. Data and Methods

2.1. Satellite Data

SMOS is a Sun-synchronous polar-orbiting satellite mission equipped with an interferometric radiometer. Its orbit covers the entire globe with a 3-day repeat cycle. SSS (and soil moisture) is retrieved across a 1,600-km-

wide swath. The unprecedented spatial resolution, of the order of 50 km, has already proven quite useful in detecting SSS eddy patterns and meanders in the Gulf Stream region (Reul et al., 2014) and in the frontal region of the Azores current (Kolodziejczyk et al., 2015). The 4-day and 25-km gridded SMOS SSS data set, smoothed with a 9-day Gaussian filter and with a 25-km median filter, was used here to assess the SSS eddy signature. This gridded product was generated by the LOCEAN (*Laboratoire d'Océanographie et du Climat: Expérimentations et Approches Numériques*) expertise center of the CATDS (*Centre Aval de Traitement des Données SMOS*). We used the so-called SMOS SSS CEC-LOCEAN L3 debiased-v2 version (Boutin et al., 2017; see the URL link in the Acknowledgements) that has improved filters for outliers and reduced systematic biases, especially close to the coasts (Boutin et al., 2018). The effective spatial resolution of this product is of the order of 75 km. The standard deviation of the difference between these SMOS SSS fields and volunteer observing ship SSS at a similar spatial resolution is 0.28 (farther than 800 km from the coast). Additional comparisons with Argo SSS data are given in section 2.2. While SMOS was launched in November 2009, we only use data from July 2010 to December 2016 since the instruments and the orbit were in a commissioning/testing phase until June 2010, potentially corrupting data quality.

The daily and ¼° gridded sea level anomalies (SLA) distributed by the CMEMS (*Copernicus Marine and Environment Monitoring Service*; see the Acknowledgements for details) were used to automatically detect and characterize mesoscale eddies. Started in November 1992, the SLA gridded field is constructed by optimally merging measurements of multiple altimeter missions (see Ducet et al., 2000). To be consistent with the SMOS data processing, the 2010–2016 and ¼° and daily SLA data set was further smoothed with a 9-day Gaussian filter (with one standard deviation equals to 3 days) to remove unanalyzed small time scale variability and then subsampled every 4 days.

In order to detect eddy-induced SSS changes and remove the large-scale and seasonally varying SLA and SSS changes not associated with eddies, the 4-day SLA and SSS maps were high-pass filtered in space and time with a 6° × 6° longitude-latitude and 120-day Hanning filters, respectively. Sensitivity tests using slightly different filter spatial lengths in longitude and latitude (as in Chelton, Schlax & Samelson, 2011, or Dufois et al., 2014) have shown no significant effects on our results. Eddy-induced SSS anomalies were computed by colocalizing eddies detected on SLA (as discussed below in section 2.3) and high-pass-filtered SSS anomalies. Unless otherwise stated, SLA and SSS anomalies discussed below refer to high-pass-filtered values.

2.2. Argo and SST Data

The mean eddy vertical structure was also investigated using vertical salinity profiles acquired by Argo floats in the tropical Pacific over the 2010–2016 time period (Roemmich & Owens, 2000). The related salinity profiles, $S(z)$, were obtained from the Coriolis center (http://www.coriolis.eu.org), and we only retained profiles for which: (1) the quality flags are "good" or "probably good," (2) the data are available at least within 10 and 950 dbar, and (3) the depth difference between two consecutive data does not exceed a given threshold (25 m for the 0- to 150-m layer, 50 m for the 150- to 300-m layer, 75 m for the 300- to 500-m layer, and 100 m below 500 m; see Pegliasco et al., 2015). Based on these three criteria, a total of 1,449 and 488 profiles was selected in the central (4° to 12°N, 180–120°W) and eastern (2–16°N, 100–70°W) tropical Pacific regions, respectively, to be further discussed (see Figure 1). About 10% of these profiles surfaced within the retained coherent eddies analyzed here. Given the Lagrangian nature of the Argo floats and their relatively low spatial sampling (the Argo nominal array has 1 float every 3° of latitude and longitude), we could not properly high-pass filter the related salinity fields in space and time as we did for the SMOS SSS. As a makeshift solution, anomalous vertical salinity profiles associated with eddies were obtained in the central and eastern regions by subtracting, from each profile surfacing within an eddy, the average of all Argo profiles located within 100 km of the given profile and not surfacing within eddies. Other methods to compute anomalies, based on either 120-day Hanning filters, or Chaigneau et al. (2011) or Dong et al. (2014) were also tested and gave similar results. Noteworthy, the colocalized (within 0.25° and 4 days) SMOS SSS and Argo near-surface ($z \leq 5$ m) salinity compared quite well in these two regions. The correlation coefficient, root-mean-square (rms) difference, ratio of standard deviations, and mean difference for the central region are 0.88, 0.25, 1.1, and 0.02, respectively. For the eastern region, the correlation coefficient, rms difference, ratio of standard deviations, and mean difference are 0.90, 0.39, 1.0, and 0.05, respectively. The rather large rms difference in the eastern region is likely due to a vertical stratification effect (Boutin et al., 2016). Indeed, SMOS SSS is representative

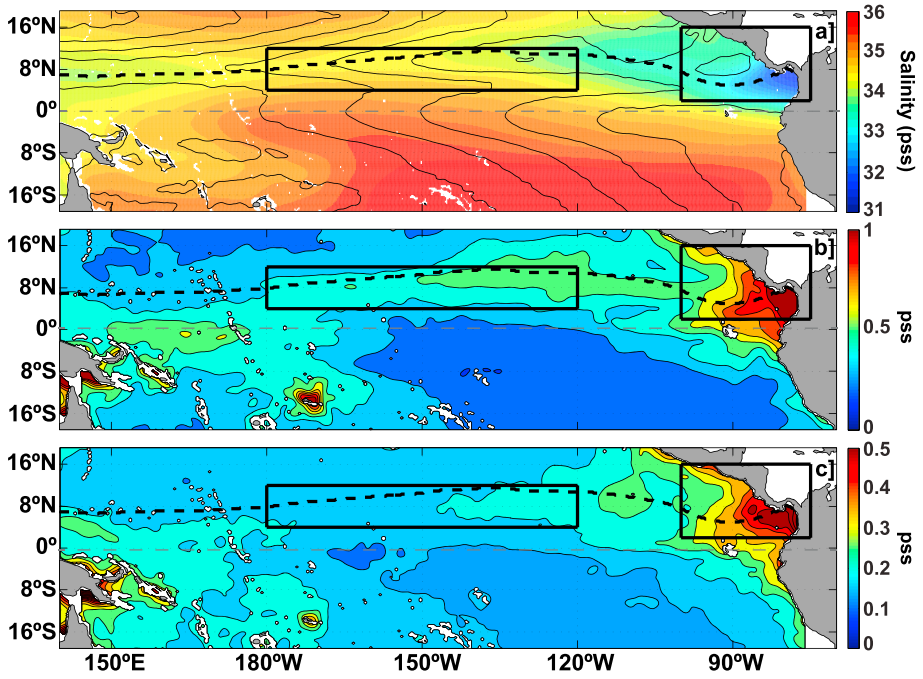

Figure 1. (a) Mean Soil Moisture and Ocean Salinity SSS and corresponding standard deviation values (color shading) denoting the (b) full and (c) mesoscale only variability, as computed from 2010 to 2016 measurements. Note that the color scale is divided by two in (c) compared to (b). The black dashed lines in all figures represent the location of minimum SSS values in the Northern Hemisphere. The two black rectangles denote the central and eastern regions discussed in the main text. Overplotted in (a) are contours of the mean dynamic topography derived from the CMEMS fields, with contour intervals equal to 10 cm. A 2° longitude/latitude smoothing was applied in (b) and (c), for clarity. pss = practical salinity scale; SSS = sea surface salinity; CMEMS = Copernicus Marine and Environment Monitoring Service.

of the first top centimeter, while Argo measurements are at several meters depth, and this region is characterized by a strong salinity stratification in the near-surface layer as will be shown later in the paper.

The high-resolution SST analysis product from Reynolds et al. (2007) combined with the SMOS SSS data was used to compute surface density. This SST product based on satellite data and in situ data from ships and buoys have a spatial grid resolution of ¼° and a temporal resolution of 1 day.

2.3. Eddy-Tracking Algorithm

As a reminder, ACE and CE are characterized by local SLA maxima and minima, and they rotate clockwise and anticlockwise in the Northern Hemisphere, respectively. Mesoscale eddies were automatically detected on high-pass-filtered SLA maps using the algorithm developed by Chaigneau et al. (2008, 2009). This SLA-based method identifies the eddy edges as the outermost closed SLA contour around local SLA extrema (minima for CEs and maxima for ACEs) associated with eddy centers. For each identified eddy, the amplitude is defined as the absolute difference value between the eddy center's SLA and the outermost SLA contour, and the eddy radius is defined as the radius of a disk having the same area as the detected eddy (Chaigneau et al., 2008). Eddy trajectories are then constructed from individual eddies detected from 4-day SLA maps using the algorithm developed and fully described in Pegliasco et al. (2015). In order to investigate the most energetic and coherent mesoscale structures, only eddies having a mean radius equal to or greater than 50 km, a mean amplitude equal to or greater than 2 cm, and a lifetime longer than 30 days were retained.

3. Results

This section describes the mean tropical Pacific SSS and its variability and mean eddy characteristics, discusses the overall SSS signature of ACE and CE, and then focuses on the composite eddy-induced SSS and $S(z)$ changes in the central and eastern parts of the tropical North Pacific.

3.1. SSS: Mean and Variability

To first set the context about SSS in the tropical Pacific, Figure 1a shows the mean SMOS unfiltered SSS (i.e., not high-pass filtered in space and time with a 6° × 6° longitude-latitude and 120-day Hanning filters, see section 2.1). We observe the well-known large-scale distribution of mean SSS as documented more than 30 years ago (e.g., Levitus, 1986). Maximum SSS values are located near the large-scale anticyclonic gyre centers (east of French Polynesian and west of Hawaiian Islands), whereas minimum SSS values are observed in a belt centered at 8–10°N beneath the Intertropical Convergence Zone and near the South Pacific Convergence Zone that extends southeastward of Papua New Guinea. The SSS minimum zone in the Northern Hemisphere (dashed line in Figure 1a) highlights the existence of a positive (negative) SSS meridional gradient to the north (south), to be further discussed.

The unfiltered SSS standard deviation map (Figure 1b) indicates that maximum SSS variability (higher than 0.5) overall coincides with the mean large-scale SSS minimum zones. These rough overlaps partly reflect the meridional displacements, at seasonal and El Niño–Southern Oscillation time scales, of the areas of large SSS meridional gradients related to the Intertropical Convergence Zone and South Pacific Convergence Zone heavy rainfall bands, as documented by Tchilibou et al. (2015). The large variability found in the equatorial band (~5°N to 5°S) and west of the dateline is mainly associated with the zonal displacements of the eastern edge of the warm and fresh pool during El Niño–Southern Oscillation (Delcroix & Picaut, 1998; Hasson et al., 2013). Also, the large variability found in the far eastern Pacific fresh pool is due to a combination of monsoon rain, trade, and gap winds and strong surface currents, as discussed in Alory et al. (2012) and Guimbard et al. (2017).

The standard deviation map of the high-pass-filtered SSS is shown in Figure 1c to assess the amplitude of the SSS mesoscale variability. The comparison between Figures 1b and 1c reveals that the SSS mesoscale variability accounts for 40% to 60% of the total SSS variability, a percentage similar to what was found for SSH (Chelton, Schlax, & Samelson, 2011), with maximum values still appearing near the SSS minimum zone in the Northern Hemisphere.

3.2. Mean Eddy Characteristics

As an illustration of the eddy detection method, Figure 2a shows the SLA map and the corresponding 326 coherent eddies (43% are ACE) identified on 5 April 2011. Some of the largest ACE and CE are located around 8–12°N in a region associated with a trough in the mean dynamic topography (see black contours in Figure 1a). This trough is associated with the strong zonal current shear between the westward flowing North Equatorial Current (~8–20°N) and the eastward flowing North Equatorial Counter Current (~3–8°N). The associated high-pass-filtered SSS anomalies are shown in Figure 2b for the eastern part of the tropical North Pacific, indicating that some (but not all) eddies have a somewhat complex SSS signature at that time.

The main eddy properties are summarized in Table 1 for the whole analyzed period. A total of 72,202 CE realizations and 57,792 ACE realizations was detected on the SLA maps within 19°N to 19°S and 150°E to 70°W, corresponding to 2,739 CE and 2,171 ACE trajectories, respectively. Little seasonality in the number of eddies and trajectories was found, possibly because the alternating periods of strong La Niña and El Niño events from 2010 to 2016 mask that seasonality. On average, over the whole tropical Pacific, the mean eddy amplitude, radius, lifetime, and rotational speed (within the radius R of the eddies) are approximately 4 cm, 110 km, 140 days, and 10–15 cm/s, respectively, with slight differences between CE and ACE properties (Table 1). Noteworthy, the probability distribution (not shown here) of these four properties is not symmetric but positively skewed. Using two practical indices of asymmetry, we note that about 55% to 70% of the values are lower than the mean, and differences between the mean and the median values normalized by the standard deviation are of the order of 0.25 (Table 1). This result is consistent with previous studies characterizing mesoscale eddies in other parts of the world ocean (e.g., Melnichenko et al., 2017).

The spatial distribution of the mean radius and amplitude (Figure 3) indicates that the largest values appear roughly in the central basin within about 4–8°N and off Central America (and 4–8°S for the ACE, not discussed here). Previous results show that the main mechanisms accounting for the large eddy radius and amplitude in these two areas are (i) the strong shear between the North Equatorial Current, the North Equatorial Counter Current, and the South Equatorial Current (extending from 20°S to 3°N) in the

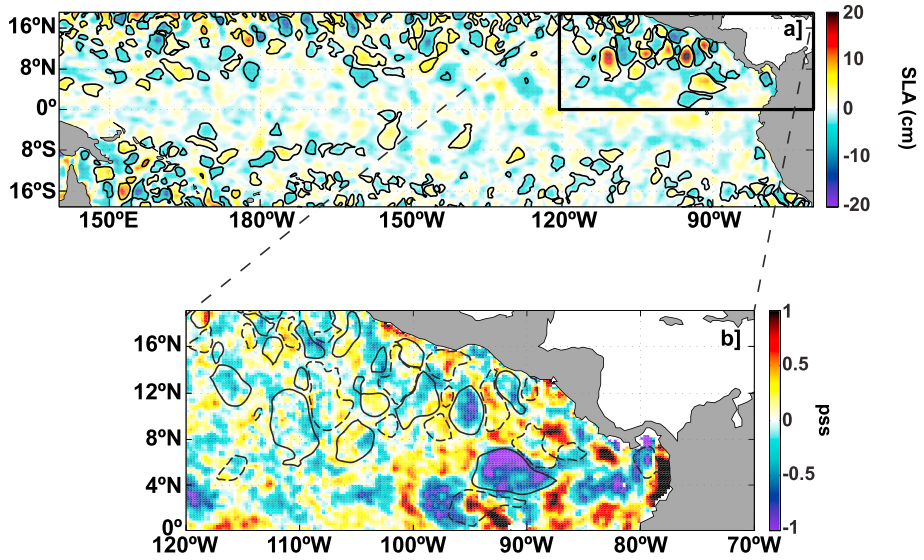

Figure 2. (a) SLA (cm) and detected mesoscale eddies on 5 April 2011; positive (negative) SLA closed contours denote anticyclonic (cyclonic) eddies. (b) Colocalized sea surface salinity anomalies (color shading) observed in the eastern region; full and dashed closed contours denote anticyclonic and cyclonic eddies, respectively. SLA = sea level anomalies; pss = practical salinity scale.

central region (Flament et al., 1996; Ubelmann & Fu, 2011), as seen from the surface dynamic topography shown in Figure 1a, and (ii) the strong intermittent transoceanic wind jets blowing from the Atlantic to the Pacific in the eastern region (Willet et al., 2006). Major differences between ACE and CE amplitudes are observed in the eastern Pacific, with ACEs being much more intense than CEs (Figures 3c and 3d).

3.3. Mean SSS Signature in ACE and CE

The spatial distribution of the mean SSS anomalies collocated with all detected long-lived (>30 days) coherent CE ranges within −0.2 to +0.2 (Figure 4a). We observe maximum negative and positive anomalies in the central and eastern parts of the tropical North Pacific, respectively, noting that these two regions roughly straddle the SSS minimum zone. Noteworthy, the spatial distribution of the mean SSS anomalies collocated with all detected ACE (Figure 4b) is almost identical, however, with a reverse sign. The spatial correlation between the mean SSS anomalies collocated with CE (Figure 4a) and ACE (Figure 4b) is of −0.65. The regionally contrasted eddy-related SSS signatures strongly suggest that different physical mechanisms are at work in the central and eastern parts of the tropical North Pacific. As a matter of fact, Figure 4c reveals that the temporal correlation between SLA (an alias of pycnocline depth in the tropics; Rébert et al., 1985)

Table 1
Mean Cyclonic (CE) and Anticyclonic (AE) Eddy Properties in the Full Analyzed Domain (19°N–19°S; 150°E–70°W) and in the Central (4° to 12°N, 180–120°W) and Eastern (2–16°N, 100–70°W) Regions (See Figure 1)

	N		*N*traj		Amplitude (cm)		Radius (km)		Lifetime (days)		Rotational speed (cm/s)	
Zone	CE	AE	CE	AE	CE	ACE	CE	ACE	CE	ACE	CE	ACE
19°N to 19°S; 150°E to 70°W	72,202	57,792	2,739	2,171	3.8 (0.25) 62%	3.7 (0.26) 65%	108 (0.17) 57%	110 (0.17) 57%	143 (0.38) 69%	145 (0.34) 68%	13.2 (0.20) 59%	12.6 (0.23) 62%
Central region	4,633	3,570	316	221	3.3 (0.20) 59%	3.4 (0.27) 63%	136 (0.15) 56%	142 (0.19) 57%	157 (0.37) 72%	157 (0.33) 70%	13.8 (0.17) 57%	13.4 (0.24) 59%
Eastern region	3,841	3,269	206	176	4.6 (0.28) 62%	6.5 (0.35) 66%	111 (0.17) 56%	122 (0.17) 55%	139 (0.37) 68%	142 (0.32) 67%	20.2 (0.19) 58%	22.7 (0.20) 58%

Note. *N* is the number of eddies, and *N*traj the number of eddy trajectories. Values in parentheses for the amplitude, radius, lifetime, and rotational speed denote the differences between the mean and median normalized by the standard deviation. Values in percentage denote the accumulated probability below the mean value.

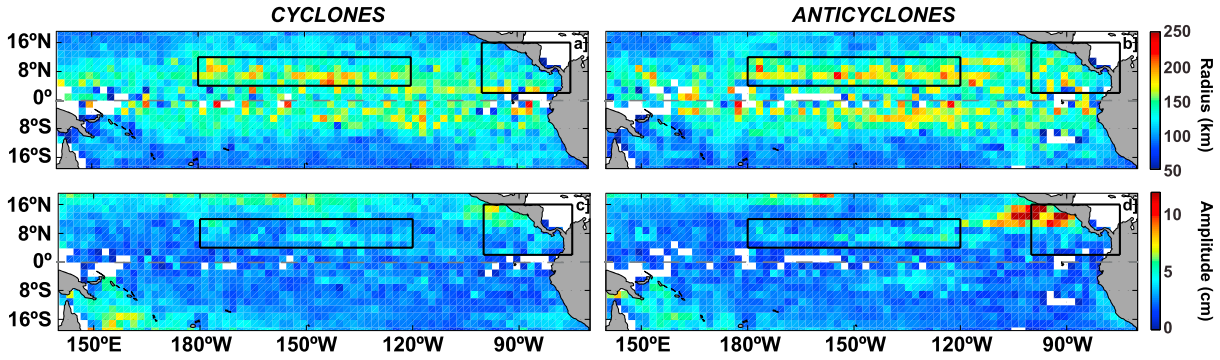

Figure 3. (a, b) Mean radius (km) and (c, d,) amplitude (cm) of (left column) cyclonic and (right column) anticyclonic eddies per 2° longitude/latitude area, averaged over July 2010 to December 2016. The two black rectangles are as in Figure 1.

and SSS anomalies is positive in the central region and negative in the eastern region, suggesting that influence from subsurface waters are much more pronounced in the latter. In the eastern Pacific, high-salinity subsurface water would be uplifted toward the surface in the core of surface-intensified CE, generating positive SSS anomalies collocated with negative SLA, while positive SLA anomalies associated with surface-intensified ACEs would result in a depressed pycnocline and consequently a reduced influence of high-salinity subsurface waters, resulting in negative SSS anomalies for ACE. The absence of this negative correlation between SLA and SSS anomalies in the central region suggests that other processes are more important in this area. We next restrict our attention to these two significant regions delimited by the two rectangles in Figure 1.

3.4. Composites in the Central and Eastern Parts of the Tropical North Pacific

3.4.1. SLA and SSS Composites

About 8,200 coherent eddy realizations were detected in the central region and 7,100 in the eastern region during the whole analyzed period (about 45% are ACE). On average, CE and ACE crossing the central region

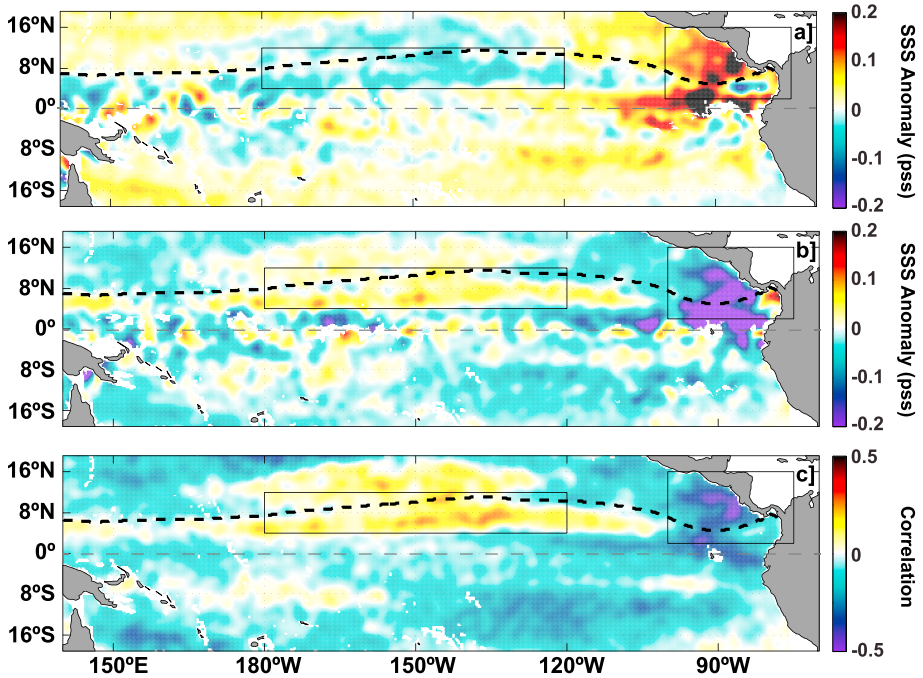

Figure 4. SSS anomalies averaged within all detected (a) cyclonic and (b) anticyclonic eddies. (c) Temporal correlation coefficients between high-pass-filtered sea level anomalies and SSS anomalies. Values were computed over 2010–2016. The two black rectangles are as in Figure 1. pss = practical salinity scale; SSS = sea surface salinity.

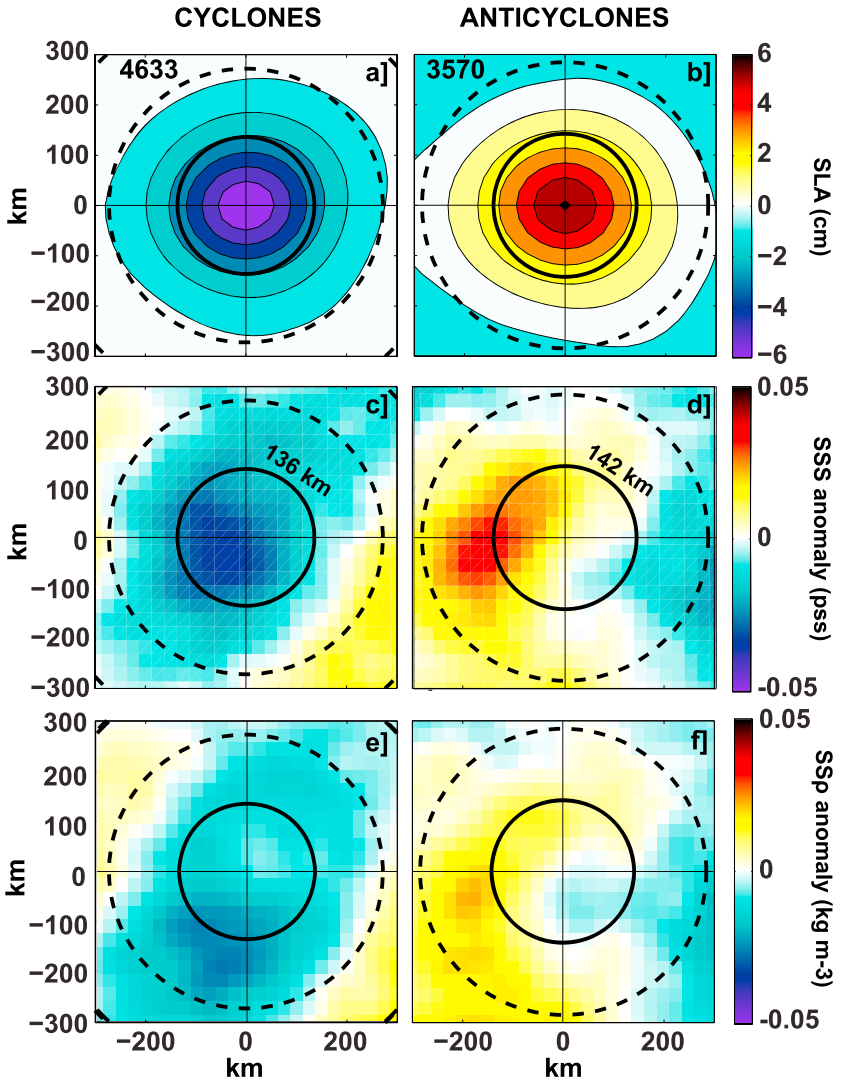

Figure 5. Composite averages of eddy-induced (a, b) sea level, (c, d) SSS, and (e, f) surface density anomalies for the (a, c, and e) cyclonic and (b, d, and f) anticyclonic eddies detected in the central region (as denoted by the larger rectangle in Figure 1). Values in (c) and (d), and (e) and (f) were computed in a rotating coordinate system where $\partial S/\partial y$ was directed to a polar angle of −90°. Numbers in the upper left quadrants in (a) and (b) represent the number of eddies used to compute the related composites. Numbers in (c) and (d) denote the mean eddy radius (km) delimited by the heavy lines. The heavy dashed lines in all panels correspond to two eddy radii. SLA = sea level anomalies; SSS = sea surface salinity.

have larger radii (+20%) and longer lifetimes (+10%) than the ones crossing the eastern region. In contrast, eddies have larger amplitudes (+40% for CE, +90% for ACE) in the eastern region, which combined with smaller radii, leads to eddies characterized by higher vorticities and rotational speeds (+45% for CE, +70% for ACE). Details about the main eddy properties in the two regions are given in Table 1.

We computed the mean composite eddy SLA and SSS anomalies in the two regions using a rotated coordinate frame where the large-scale SSS meridional gradient (∂SSS/∂y) is directed to a polar angle of −90°, as is found south of about 8°N. We adopted such an approach, following Gaube et al. (2015), to highlight the role of horizontal advection in regions that include opposite SSS meridional gradients, such as in the central region where ∂SSS/∂y reverses across the minimum SSS zone (Figure 1a). The eddy-induced SLA and SSS anomaly composites are presented in physical coordinates in Figures 5a–5d for the central region and in Figures 6a–6d for the eastern region. Given the large number of detected eddies and trajectories (Ntraj, see Table 1), the uncertainty in the composites is small (with a standard error of the order of $\frac{0.3}{\sqrt{N_{\text{traj}}}}$ for SSS) and hence the differences between

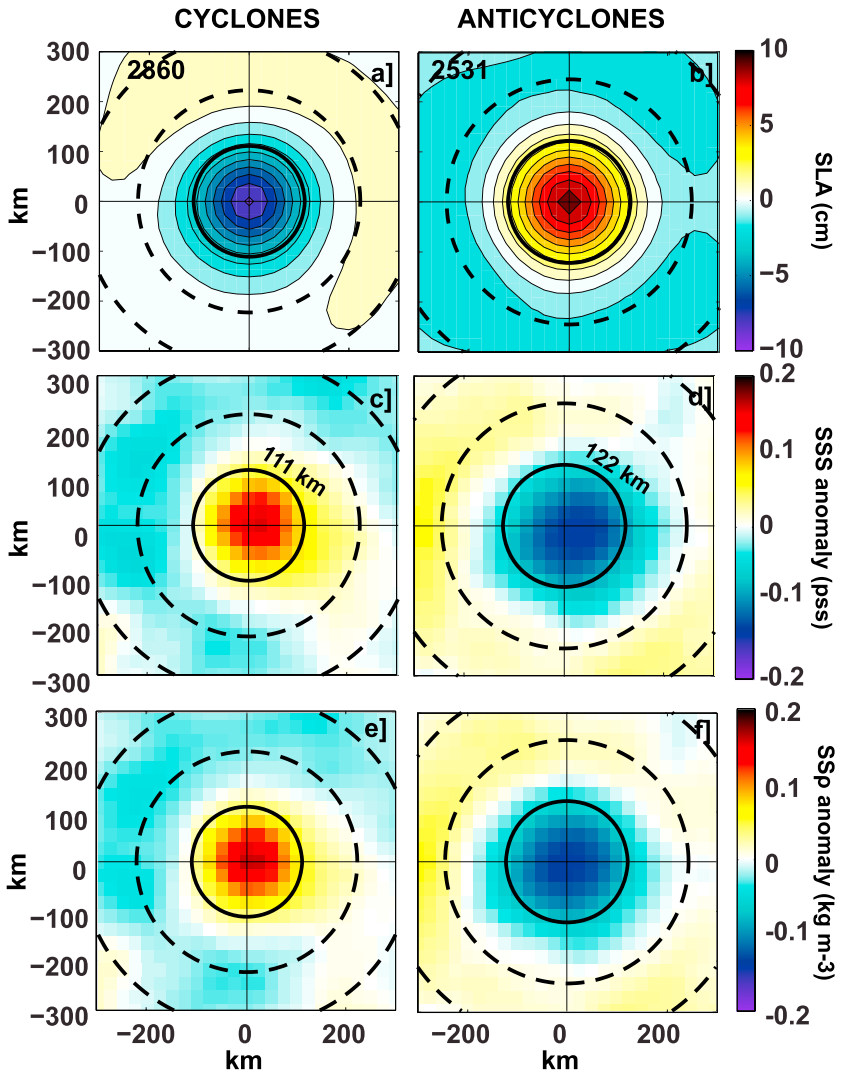

Figure 6. Same as Figure 5 but for eastern region (denoted by the smaller rectangle in Figure 1). SLA = sea level anomalies; SSS = sea surface salinity.

ACE and CE composites are significant. The corresponding sections (crossing the eddy center at $Y = 0$) of the SSS and swirl geostrophic velocity anomalies are shown in Figures 7a and 7b. (Note that using normalized instead of physical coordinates did not change our main conclusions for the SSS composites.) There, the swirl velocity was computed assuming geostrophy and using the SLA composite (e.g., Figures 5a and 5b, and 6a and 6b), with the Coriolis parameter (f) calculated using the mean latitude of all eddy centers in each subregion. One may question the use of geostrophy for regions close to the equator, especially for the southern part of the eastern region. This potential shortcoming is discussed in the last section.

The averaged eddies of the central region have a maximum SLA of the order of 6 cm and a radius of about R = 140 km (Figures 5a and 5b). The spatial distribution of the SLA has a near Gaussian shape, with maximum value centered at the eddy core and a zero crossing at a distance of about $2R$. The eddy-induced SSS composites exhibit a somewhat dipole-like pattern (clearer for the ACE) with a tendency to have opposite SSS anomalies in the leading edge (i.e., western side when $\partial SSS/\partial y$ is directed to a polar angle of $-90°$) of the eddy as compared to the trailing edge, as well as clear opposite SSS anomalies for the ACE and CE (Figures 5c and 5d, see also Figure 7a). There is also a slight tendency for the larger anomalies to be located on the leading edge of the ACE and CE. As discussed in Chelton, Gaube, et al. (2011), the dipole-like pattern is indicative of horizontal advection and the leading/trailing edge asymmetry would occur because the eddy trailing edges tend to come across a

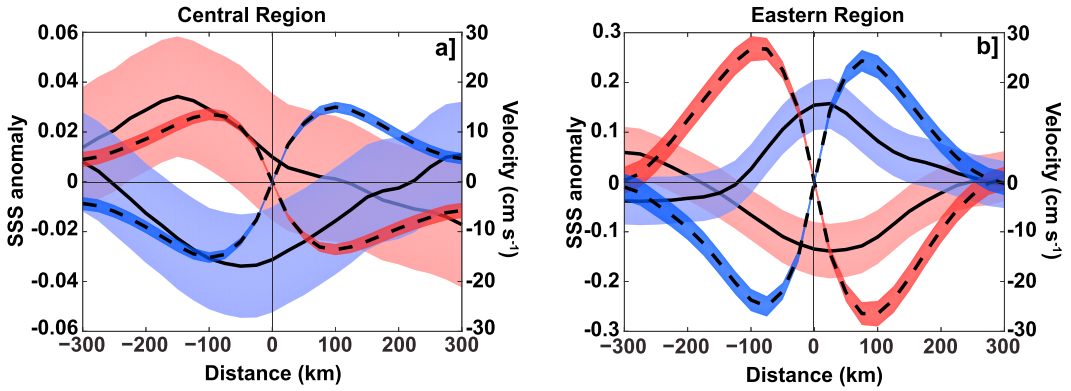

Figure 7. Zonal sections across the composite averages of (a) the central region in Figure 5 and (b) the eastern region in Figure 6. Full lines denote sea surface salinity (SSS) anomalies scaled on the left axes, and dashed lines denote swirl velocity anomalies scaled on the right axes. Full and dashed black lines with red (blue) envelopes representing the standard errors are for anticyclonic (cyclonic) eddies.

$\partial SSS/\partial y$ recently reduced by the eddy leading edges. The central region composites hence could emphasize the likely role of horizontal advection that combines the rotational sense of the ACE and CE and the $\partial SSS/\partial y$ direction, as shown schematically in Figure 8.

The eastern region averaged eddies have a maximum SLA of the order of 10 cm, that is, about 65% larger than for the central region, and a radius R of 110 to 120 km (Figures 6a and 6b). The spatial distribution of the SLA also exhibits a near Gaussian shape, although with a tendency (especially for the ACE) to have opposite SLA values outside of one eddy radius (note that this tendency is slightly reduced when using normalized coordinates). Contrasting with the central region, the eastern region SSS composites (Figures 6c and 6d) reveal a monopole-like structure in which the SSS anomalies are almost symmetrical about—and maximum at—the eddy centers. There, the ACE and CE composites are nearly mirror images with a sign reversal, and the SSS anomalies are 2–4 times larger and opposite to those found in the central region (see Figures 5c and 5d). Given the regional 10- to 20-m-shallow mixed-layer depth (e.g., Alory et al., 2012; Delcroix et al., 1996), the eastern region SSS composites would thus support one of the classical views of expected eddy effects. Namely, that in the absence of winds and during their growth phase, surface-intensified CE would tend to upwell (or mix) high-salinity subsurface waters into the surface layer generating positive SSS anomaly, and inversely for ACE (see schematic in Figure 8). The eastern region eddy-induced SSS anomalies could then likely highlight the leading role of vertical processes. There are, however, other possible explanations, notably those involving the occurrence of more energetic eddies in the eastern versus central region; these are discussed in section 4.

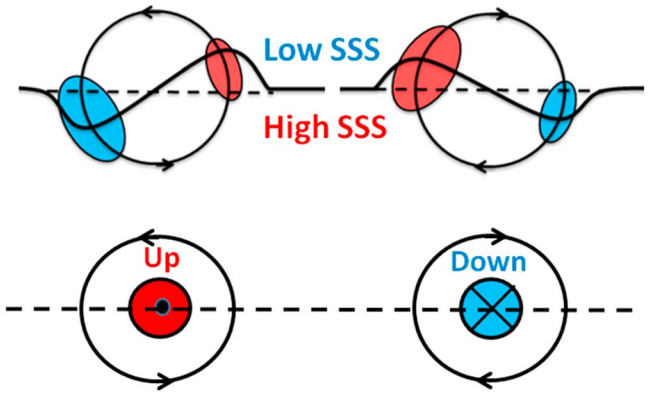

Figure 8. Schematic diagrams of eddy-induced (top panels) horizontal and (bottom panels) vertical advection of salinity gradient by (left panels) anticyclonic and (right panels) cyclonic eddies. The top panels would apply for the central region, the bottom panels for the eastern regions (see Figure 1). SSS = sea surface salinity.

3.4.2. Surface Density and Vertical Salinity Composites

Combining SSS data from SMOS and SST data from Reynolds et al. (2007), we computed the eddy-induced surface density (ρ) anomaly, also using the rotated coordinate frame where the salinity meridional gradient ($\partial SSS/\partial y$) is directed to a polar angle of −90°. The eddy-induced density anomaly patterns (Figures 5e and 5f and 6e and 6f) resemble the corresponding SSS anomaly patterns in both regions, indicating the dominant effect of SSS on surface density patterns. Of note, computation of the eddy-induced SST anomaly patterns (not shown here) shows the amplitude of the density patterns are, however, slightly reduced by the SST patterns in the central region (same signs in SST, SSS, and ρ) and slightly enhanced in the eastern region (same signs in SSS and ρ, and opposite sign in SST). The dipole-like and monopole-like structures are even enhanced in surface density as compared to SSS in the central (Figures 5e and 5f) and eastern (Figures 6e and 6f) regions, respectively. The surface density anomaly has maximum amplitude of

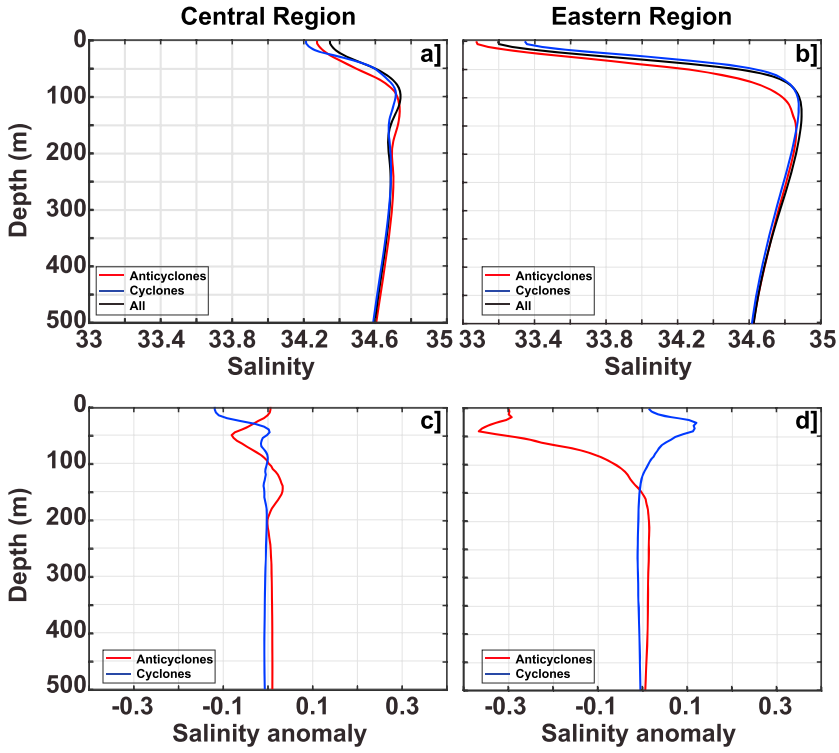

Figure 9. (top) Mean salinity profiles in the (a) central and (b) eastern regions (see Figure 1). (bottom) Eddy-induced salinity anomalies in the (c) central and (d) eastern regions. Black curves in (a) and (b) are computed from all Argo floats, red curves in (a)–(d) from Argo floats surfacing in anticyclonic eddies only, and blue curves in cyclonic eddies only.

the order of ±0.15 kg/m^3 in the eastern region, which is about 3–4 times higher than in the central region.

The relative sign of the eddy-induced SLA and corresponding surface density can be used to infer qualitative information on the eddy vertical structure (see Assasi et al., 2016). Physically, for instance, ACE are always associated with positive SLA (as in Figures 5b and 6b), while the surface density anomaly is expected to be negative for surface-intensified ACE and positive when the eddy core is in subsurface, and vice versa for the CE (see Figure 2 of Assasi et al., 2016, for a schematic). Noting this difference is interesting here because we found opposite sign in SLA and ρ in the eastern region (both for CE and ACE), whereas we tend to have the same sign in SLA and ρ in the central region (at least for the CE, not that clear for the ACE). This suggests occurrence of surface-intensified eddies in the eastern region and subsurface-intensified eddies in the central region. To test this hypothesis, we also computed the eddy-induced $S(z)$ composites derived from Argo floats in both regions. The composites $S(z)$ show the largest anomalies in the upper 50 m in the eastern region (Figures 9b and 9d), whereas the perturbations do not seem to preferentially appear within the upper 200 m in the central region (Figures 9a and 9c), making it difficult to reach a firm conclusion. Whether or not this is due to the inability to properly high-pass filter the Argo salinity profiles due to their too poor time/space sampling remains to be elucidated.

3.5. Estimating the Eddy SSS Meridional Salt Transport

Following the approach of Haussmann and Czaja (2012) for the transport of heat, we computed the meridional transport of fresh water (F) associated with the central and eastern regions eddy composites as in Melnichenko et al. (2017):

$$F = -\frac{h}{S_0}\int_{-L}^{L} v'.s'\,\mathrm{d}x \tag{1}$$

where h is the mixed-layer depth estimated from climatology (see Figure 4 in Delcroix et al., 1996), s' and v' the eddy composite anomalous SSS and meridional velocity of Figures 7a and 7b, S_0 the mean SSS

Table 2
Eddy-Induced Meridional Transport of Fresh Water (m^3/s) Multiplied by −1 for the Central and Eastern Regions (See Figure 1) as Determined From Equation (1)

			$L = R$		$L = 2R$	
Region	h (m)	So	CE	AE	CE	AE
Central region	35	34.0	203 (742)	348 (836)	351 (1,323)	790 (1,511)
Eastern region	10	33.1	244 (773)	251 (978)	542 (1,324)	431 (1,642)

Note. Values in parentheses denote the standard errors.

determined from the SMOS data set (as in Figure 1a), and L the integration length bracketing the eddy composite center. The eddy-related meridional transport of fresh water is given in Table 2 for the central and eastern regions with values of $L = R$ and $L = 2R$. As inferred from the antisymmetric shape of the meridional velocity of Figures 7a and 7b, the integration over $L = \pm R$ or $L = \pm 2R$ closely verifies that the mean meridional mass transport across the eddy is 0 (where R is the mean eddy radius given in Table 1). Noteworthy, as discussed above, the eddy-induced SSS composites in Figures 7a and 7b were determined using a rotated coordinate frame where the large-scale SSS meridional gradient ($\partial SSS/\partial y$) was directed to a polar angle of −90°. Hence, the "meridional" transport of fresh water given in Table 2 must be viewed as a transport parallel to the large-scale SSS meridional gradient (see Figure 1a). Values of F in Table 2 range within −200 and −800 m^3/s, depending on the region and on the CE or ACE contributions, with error bars 2–3 times as much. To put this eddy composite contribution in perspective, one would first need to have much smaller error bars and second to compute all terms of the surface fresh water (or salinity) budget. We believe all those terms are quantifiable only with realistic high-resolution model outputs (as in Tréguier et al., 2012) and not with the observations we have in hand. However, for comparison purposes, we note that our values of F are about twice as much as values found in the subtropical North Atlantic (Melnichenko et al., 2017).

4. Conclusion

A large amount of literature has been published on mesoscale variability and eddies in the last decades, mostly since the advent of satellite altimetry and trustworthy eddy-resolving simulations. Despite this, aside from the recent studies of Reul et al. (2014) and Melnichenko et al. (2017), little has been found yet regarding the observations and interpretation of eddy-induced salinity changes, notably in the tropics. Findings of the present study, which focuses on the tropical Pacific Ocean and relies on both SLA altimetry measurements and the unprecedented and basin-scale high-resolution SSS measurements derived from SMOS since the mid-2010s, usefully complement those of earlier studies.

Our results first indicate that the SSS mesoscale variability accounts for as much as 40% to 60% of the total SSS variability from 2010 to 2016. They further reveal that the most pronounced and consistent eddy-related SSS perturbations, of the order of ±0.2, occur in the central and eastern parts of the tropical North Pacific region. In the central part we observe the largest eddy radii and meridional gradients of SSS, while in the eastern part we observe larger amplitude eddies and largest near-surface vertical salinity gradients. In the central part, composites of eddy-induced SSS changes reveal a dipole-like pattern, also detected in density, with maximum anomaly on the leading edge of the westward propagating eddy, while in the eastern part composites show a monopole-like pattern centered in the eddy core. The contrasting dipole/monopole patterns between the central and eastern region composites suggest that the two mechanisms that explain these patterns are horizontal advection and vertical processes, respectively.

Interpreting the monopole structure of the salinity composites in the eastern region as an evidence of vertical processes may actually be more complex than simply suggested here. Another possible explanation for the monopole structure would be that the more energetic eddies in this region (compared with the central region) are more effective at trapping anomalously high or low salinity water in the nonlinear cores of the eddies. For instance, Gaube et al. (2015) show how SST composites can evolve from a dipole structure for small-amplitude eddies to a monopole structure for large-amplitude eddies. It may also be

the case for SSS of the energetic eddies (especially ACEs) in the eastern region (see Table 1). A future study focusing on the monopole structure should thus be undertaken. Such a study would also need to discriminate the respective role of different physical processes that lead to the vertical advection of subsurface waters, if any (see Gaube et al., 2015, and the references therein). These processes involve (i) surface vorticity effect and (ii) eddy air sea flux feedbacks into Ekman pumping. The respective contributions of all these processes and how they vary in time depending on the eddy age, amplitude, growth, or decay as well as on the background wind field and SST gradients clearly need further clarification.

As noted in section 3.4.1, the use of geostrophy to characterize the surface velocity field from SSH may be questionable, in particular, for near-equatorial regions. Comparisons made in the Pacific Ocean between direct equatorial current measurements and geostrophic velocities derived from SSH indicate that the variability of the equatorial currents are reasonably well represented by geostrophy for periods greater than one month and with a 1–2° latitudinal scale (e.g., Delcroix et al., 2000; Picaut et al., 1990). These comparisons, right at the equator, represent the most stringent tests for geostrophy given the high sensibility of the calculation to small SSH errors.

In order to test the validity of the geostrophic assumption, in particular, in the eastern region located close to the equator, we computed for each retained eddy, the Rossby number as follows:

$$R_0 = \frac{U_{\max}}{f\,R} \tag{2}$$

where $U_{\max}$ is the maximum swirl velocity of the eddy, f the Coriolis parameter at the eddy center, and R the eddy radius. R_0 characterizes the dynamical balance of eddies, with $R_0 \sim 1$ ($R_0 \ll 1$, respectively) indicating an eddy in cyclostrophy (quasi-geostrophic) balance (Cushman-Roisin & Beckers, 2011; Rudnick et al., 2015). Note that these Rossby number estimates remain imperfect as the (unavailable) total rather than swirl geostrophic velocity should have been used in the R_0 computation.

In the eastern region, about 83% (31%, respectively) of the 7,100 (~480) eddies detected between 2°N and 16°N (2–5°N) have a $R_0 < 0.2$, indicating that our composites analysis may partly be biased by ageostrophic eddies mainly located south of ~5°N. Close to the equator, nonlinear effects like cyclostrophy, which is a dynamical balance between the pressure gradient and the centrifugal force of a curved flow, modify the geostrophic momentum balance of the eddies (e.g., Cushman-Roisin & Beckers, 2011). This is in agreement with the findings of Qiu et al. (2017, 2018) that suggested, based on high-resolution observations and a global ocean model, that unbalanced motions dominate scales as large as 250–500 km in the tropical Pacific. About 55% of the eddies considered here have radii of 50–140 km (Table 1), corresponding to length scales of 200–560 km, and are thus likely influenced by the divergent component of the flow. Also, Amores et al. (2018) showed that current gridded altimetry products underestimate the number of small-scale eddies, while they overestimate the density of large-scale eddies. This adds another reason for caution with the degree of accuracy of the composite analyses, especially in the eastern region of the tropical Pacific, where some of our results (e.g., horizontal advection and salt fluxes) might be influenced by a significant nongeostrophic component of the flow field. Further analyses, notably based on the next generation Surface Water and Ocean Topography interferometric satellite with higher SSH resolution (Fu & Ubelmann, 2014), will help to refine the present conclusion.

Despite these novel results, there are still numerous unanswered questions, notably regarding (i) the respective contribution of all other factors affecting the high-frequency surface layer salinity (or fresh water) variability that we were not able to quantify with the available observations and (ii) causes for the diversity of the eddy-induced SSS changes we detected outside of the tropical North Pacific region. In partly addressing these issues, our investigation of high-pass-filtered precipitation (and assumed derived SSS) changes colocalized with eddies proves inconclusive (using the TRMM3B42 product). Hence, there is abundant room for further progress in quantifying all factors affecting eddy-induced SSS changes and their role in the mixed-layer salinity budget. Dedicated analyses of eddy-resolving simulations, validated with the present observed features, are clearly good candidates for further clarification. The use of coupled simulations could also shed light on the likelihood of eddy-induced combined SSS, SST and atmospheric perturbations.

Acknowledgments

We benefited from the SLA by the CMEMS (http://marine.copernicus.eu/); we used the product identifier: SEALEVEL_GLO_PHY_L4_REP_OBSERVATIONS_008_047). The SMOS SSS is made available by the CATDS (https://www.catds.fr/); we used the L3_DEBIAS_LOCEAN_v2 SSS maps, which have been produced by LOCEAN and ACRI that participate to the Ocean Salinity Expertise Center of CATDS (see http://www.catds.fr/Products/Available-products-from-CEC-OS/L3-Debiased-Locean-v2). This work is a contribution to the TOSCA-SMOS proposal supported by CNES. Three of us (T. D., A. C., and D. S.) were supported by IRD as part of its capacity building politics in western Africa. We also wish to thank G. Alory for fruitful discussions and the ICPMA-UNESCO Chair where this work started a few months ago. Fruitful comments from D. Chelton and anonymous reviewers were much appreciated.

References

Alory, G., Delcroix, T., Téchiné, P., Diverrès, D., Varillon, D., Cravatte, S., et al. (2015). The French contribution to the voluntary observing ships network of sea surface salinity. *Deep Sea Research*, *105*, 1–18. https://doi.org/10.1016/j.DSR.2015.08.005

Alory, G., Maes, C., Delcroix, T., Reul, N., & Illig, S. (2012). Seasonal dynamics of sea surface salinity off Panama: The far eastern Pacific fresh pool. *Journal of Geophysical Research*, *117*, C04028. https://doi.org/10.1029/2011JC007802

Amores, A., Jordà, G., Arsouze, T., & Le Sommer, J. (2018). Up to what extent can we characterize ocean eddies using present-day gridded altimetric products? *Journal of Geophysical Research: Oceans*, *123*, 7220–7236. https://doi.org/10.1029/2018JC014140

Assasi, C., Morel, Y., Vandermeirsch, F., Chaigneau, A., Pegliasco, C., Morrow, R., et al. (2016). An index to distinguish surface- and subsurface-intensified vortices from surface observations. *Journal of Physical Oceanography*, *46*(8), 2529–2552. https://doi.org/10.1175/JPO-D-15-0122.1

Boutin, J., Chao, Y., Asher, W. E., Delcroix, T., Drucker, R., Drushka, K., et al. (2016). Satellite and in situ salinity: Understanding stratification and sub-footprint variability. *Bulletin of the American Meteorological Society*, *97*(8), 1391–1407. https://doi.org/10.1175/BAMS-D-15-00032

Boutin J., Vergely, J. L., & Khvorostyanov, D. (2017). SMOS SSS L3 debias v2 maps generated by CATDS CEC LOCEAN. 2.0 version. SEANOE. https://doi.org/10.17882/52804#54823

Boutin, J., Vergely, J. L., Marchand, S., D'Amico, F., Hasson, A., Kolodziejczyk, N., et al. (2018). New SMOS sea surface salinity with reduced systematic errors and improved variability. *Remote Sensing of Environment*, *214*, 115–134. https://doi.org/10.1016/j.rse.2018.05.022

Chaigneau, A., Eldin, G., & Dewitte, B. (2009). Eddy activity in the four major upwelling systems from satellite altimetry (1992–2007). *Progress in Oceanography*, *83*(1-4), 117–123. https://doi.org/10.1016/j.pocean.2009.07.012

Chaigneau, A., Gizolme, A., & Grados, C. (2008). Mesoscale eddies off Peru in altimeter records: Identification algorithms and eddy spatio-temporal patterns. *Progress in Oceanography*, *79*(2-4), 106–119. https://doi.org/10.1016/j.pocean.2008.10.013

Chaigneau, A., Le Texier, M., Eldin, G., Grados, C., & Pizarro, O. (2011). Vertical structure of mesoscale eddies in the eastern South Pacific Ocean: A composite analysis from altimetry and Argo profiling floats. *Journal of Geophysical Research*, *116*, C11025. https://doi.org/10.1029/2011JC007134

Chelton, D. B., Gaube, P., Schlax, M. G., Early, J. J., & Samelson, R. M. (2011). The influence on nonlinear eddies on near-surface oceanic chlorophyll. *Science*, *334*(6054), 328–332. https://doi.org/10.1126/science.1208897

Chelton, D. B., Schlax, G. S., & Samelson, R. M. (2011). Global observations of nonlinear mesoscale eddies. *Progress in Oceanography*, *91*(2), 167–216. https://doi.org/10.1016/j.pocean.2011.01.002

Chelton, D. B., Schlax, M. G., Samelson, R. M., & de Szoeke, R. A. (2007). Global observations of large oceanic eddies. *Geophysical Research Letters*, *34*, L15606. https://doi.org/10.1029/2007GL030812

Cushman-Roisin, B., & Beckers, J. M. (2011). *Introduction to geophysical fluid dynamics, physical and numerical aspects* (2nd ed., Vol. 101, p. 875). Waltham, MA: Academic Press, Elsevier.

Cushman-Roisin, B., Tang, B., & Chassignet, E. P. (1990). Westward motion of mesoscale eddies. *Journal of Physical Oceanography*, *20*(5), 758–768. https://doi.org/10.1175/1520-0485(1990)020<0758:WMOME>2.0.CO;2

Delcroix, T., Dewitte, B., duPenhoat, Y., Masia, F., & Picaut, J. (2000). Equatorial waves and warm pool displacements during the 1992–1998 ENSO events. Observations and modelling. *Journal of Geophysical Research*, *105*(C11), 26,045–26,062. https://doi.org/10.1029/2000JC900113

Delcroix, T., Henin, C., Porte, V., & Arkin, P. (1996). Precipitation and sea surface salinity in the tropical Pacific. *Deep Sea Research*, *43*(7), 1123–1141. https://doi.org/10.1016/0967-0637(96)00048-9

Delcroix, T., McPhaden, M., Dessier, A., & Gouriou, Y. (2005). Time and space scales for sea surface salinity in the tropical oceans. *Deep Sea Research*, *52/5*, 787–813. https://doi.org/10.1016/j.dsr.2004.11.012

Delcroix, T., & Picaut, J. (1998). Zonal displacements of the western equatorial Pacific fresh pool. *Journal of Geophysical Research*, *103*(C1), 1087–1098. https://doi.org/10.1029/97JC01912

Dong, C., McWilliams, J. C., Liu, Y., & Chen, D. (2014). Global heat and salt transports by eddy movement. *Nature Communications*, *5*(1). https://doi.org/10.1038/ncomms4294

Ducet, N., Le Traon, P. Y., & Reverdin, G. (2000). Global high resolution mapping of ocean circulation from the combination of TOPEX/Poseidon and ERS-1/2. *Journal of Geophysical Research*, *105*(C8), 19,477–19,498. https://doi.org/10.1029/2000JC900063

Dufois, F., Hardman-Mountford, N. J., Greenwood, J., Richardson, A. J., Feng, M., Herbette, S., & Matear, R. (2014). Impact of eddies on surface chlorophyll in the South Indian Ocean. *Journal of Geophysical Research: Oceans*, *119*, 8061–8077. https://doi.org/10.1002/2014JC010164

Flament, P. J., Kennan, S. C., Knox, R. A., Niiler, P. P., & Bernstein, R. L. (1996). The 3-dimensionnal structure of an upper ocean vortex in the tropical Pacific. *Nature*, *383*(6601), 610–613. https://doi.org/10.1038/383610a0

Fournier, S., Reager, J. T., Lee, T., Vazquez-Cuervo, J., David, C. H., & Gierach, M. M. (2016). SMAP observes flooding from land to sea: The Texas event of 2015. *Geophysical Research Letters*, *43*, 10,338–10,346. https://doi.org/10.1002/2016GL070821

Fournier, S., Vialard, J., Lengaigne, M., Lee, T., Gierach, M. M., & Chaitanya, A. V. (2017). Modulation of the Ganges-Brahmaputra river plume by the Indian Ocean dipole and eddies inferred from satellite observations. *Journal of Geophysical Research: Oceans*, *122*, 9591–9604. https://doi.org/10.1002/2017JC013333

Frenger, I., Gruber, N., Knutti, R., & Münnich, M. (2013). Imprint of southern ocean eddies on winds, clouds and rainfall. *Nature Geoscience*, *6*(8), 608–612. https://doi.org/10.1038/ngeo1863

Fu, L., Chelton, D., Le Traon, P. Y., & Morrow, R. (2010). Eddy dynamics from satellite altimetry. *Oceanography*, *23-4*, 14–25.

Fu, L.-L., & Ubelmann, C. (2014). On the transition from profile altimetry to swath altimeter for observing global ocean surface topography. *Journal of Atmospheric and Oceanic Technology*, *31*(2), 560–568. https://doi.org/10.1175/JTECH-D-13-00109.1

Gaube, P., Chelton, D., Samelson, R., Schlax, M., & O'Neill, L. (2015). Satellite observations of mesoscale eddy-induced Ekman pumping. *Journal of Physical Oceanography*, *45*(1), 104–132. https://doi.org/10.1175/JPO-D-14-0032-1

Guimbard, S., Reul, N., Chapron, B., Umbert, M., & Maes, C. (2017). Seasonal and interannual variability of the Eastern Tropical Pacific Fresh Pool. *Journal of Geophysical Research: Oceans*, *122*, 1749–1771. https://doi.org/10.1002/2016JC012130

Hasson, A., Delcroix, T., & Dussin, R. (2013). An assessment of the mixed layer salinity budget in the tropical Pacific Ocean. Observations and modelling (1990-2009). *Ocean Dynamics*, *63*(2-3), 179–194. https://doi.org/10.1007/s10236-013-0596-2

Haussmann, U., & Czaja, A. (2012). The observed signature of mesoscale eddies in sea surface temperature and the associated heat transport. *Deep-Sea Research Part I*, *70*, 60–72.

Kerr, Y. H., Waldteufel, P., Wigneron, J. P., Delwart, S., Cabot, F., Boutin, J., et al. (2010). The SMOS mission: A new tool for monitoring key elements of the global water cycle. *Proceedings of the IEEE*, *98*(5), 666–687. https://doi.org/10.1109/jproc.2010.2043032

Kolodziejczyk, N., Hernandez, O., Boutin, J., & Reverdin, G. (2015). SMOS salinity in the subtropical North Atlantic salinity maximum: 2. Two-dimensional horizontal thermohaline variability. *Journal of Geophysical Research: Oceans*, *120*, 972–987. https://doi.org/10.1002/2014JC010103

Lagerloef, G., Colomb, F. R., le Vine, D., Wentz, F., Yueh, S., Ruf, C., et al. (2008). The AQUARIUS/SAC-D mission: Designed to meet the salinity remote-sensing challenge. *Oceanography*, *21*(1), 68–81. https://doi.org/10.5670/oceanog.2008.68

Lagerloef, G., Schmitt, R., Schanze, J., & Kao, H.-Y. (2010). The ocean and the global water cycle. *Oceanography*, *23*(4), 82–93. https://doi.org/10.5670/oceanog.2010.07

Le Traon, P. Y., & Morrow, R. (2001). Ocean currents and eddies. In L. L. Fu & A. Cazenave (Eds.), *Satellite altimetry and Earth science*, *International Geophysics Series* (Vol. 69, pp. 71–215). Waltham, MA: Academic Press, Elsevier.

Le Traon, P. Y., Rouquet, Y., & Boissier, C. (1990). Spatial scales of mesoscale variability in the North Atlantic as deduced from GEOSAT data. *Journal of Geophysical Research*, *95*(C11), 20,267–20,285. https://doi.org/10.1029/JC095iC11p20267

Lee, T., Lagerloef, G., Gierach, M., Kao, H.-Y., Yueh, S., & Dohan, K. (2012). Aquarius reveals salinity structure of tropical instability waves. *Geophysical Research Letters*, *39*, L12610. https://doi.org/10.1029/2012GL052232

Lee, T., Lagerloef, G., Kao, H. Y., McPhaden, M., Willis, J., & Gierach, M. (2014). The influence of salinity on tropical Atlantic instability waves. *Journal of Geophysical Research: Oceans*, *119*, 8375–8394. https://doi.org/10.1002/2014JC010100

Levitus, S. (1986). Annual cycle of salinity and salt storage in the world ocean. *Journal of Physical Oceanography*, *16*(2), 322–343. https://doi.org/10.1175/1520-0485(1986)016<0322:ACOSAS>2.0.CO;2

Ma, X., Jing, Z., Chang, P., Liu, X., Montuoro, R., Small, R. J., et al. (2016). Western boundary currents regulated by interaction between ocean eddies and the atmosphere. *Nature*, *535*(7613), 533–537. https://doi.org/10.1038/nature18640

Maes, C., Dewitte, B., Sudre, J., Garçon, V., & Varillon, D. (2013). Small-scale features of temperature and salinity surface fields in the Coral Sea. *Journal of Geophysical Research: Oceans*, *118*, 5426–5438. https://doi.org/10.1002/jgrc.20344

McGillicuddy, D. J. Jr. (2016). Mechanisms of physical-biochemical interaction at the oceanic mesoscale. *Annual Review of Marine Science*, *8*(1), 125–159. https://doi.org/10.1146/annurev-marine-010814-015606

Melnichenko, O., Amores, A., Maximenko, N., Hacker, P., & Potemra, J. (2017). Signature of mesoscale eddies in satellite sea surface salinity. *Journal of Geophysical Research: Oceans*, *122*, 1416–1424. https://doi.org/10.1002/2016JC012420

Millero, F. J. (1993). What is PSU? *Oceanography*, *6*(3), 67.

MODE Group (1978). The mid-ocean dynamics experiment. *Deep Sea Research*, *25*, 859–910.

Morrow, R., Birol, F., Griffin, D., & Sudre, J. (2004). Divergent pathways of cyclonic and anti-cyclonic ocean eddies. *Geophysical Research Letters*, *31*, L24311. https://doi.org/10.1029/2004GL020974

Pegliasco, C., Chaigneau, A., & Morrow, R. (2015). Main eddy vertical structures observed in the four major eastern boundary upwelling systems. *Journal of Geophysical Research: Oceans*, *120*, 6008–6033. https://doi.org/10.1002/2015JC010950

Picaut, J., Busalacchi, A., McPhaden, M., & Camusat, B. (1990). Validation of the geostrophic method for estimating zonal currents at the equator from GEOSAT altimeter data. *Journal of Geophysical Research*, *95*(C3), 3015–3024. https://doi.org/10.1029/JC095iC03p03015

Qiu, B., Chen, S., Klein, P., Wang, J., Torres, H., Fu, L., & Menemenlis, D. (2018). Seasonality in transition scale from balanced to unbalanced motions in the World Ocean. *Journal of Physical Oceanography*, *48*(3), 591–605. https://doi.org/10.1175/JPO-D-17-0169.1

Qiu, B., Nakano, T., Chen, S., & Klein, P. (2017). Submesoscale transition from geostrophic flows to internal waves in the northwestern pacific upper ocean. *Nature Communications*, *8*, 14055. https://doi.org/10.1038/ncomms14055

Rébert, J. P., Donguy, J. R., & Eldin, G. (1985). Relations with sea level, thermocline depth, heat content and dynamic height in the tropical Pacific Ocean. *Journal of Geophysical Research*, *90*(C6), 11,719–11,725. https://doi.org/10.1029/JC090iC06p11719

Reul, N., Chapron, B., Lee, T., Donlon, C., Boutin, J., & Alory, G. (2014). Sea surface salinity structure of the meandering Gulf Stream revealed by SMOS sensor. *Geophysical Research Letters*, *41*, 3141–3148. https://doi.org/10.1002/2014GL059215

Reul, N., Fournier, S., Boutin, J., Hernandez, O., Maes, C., Chapron, B., et al. (2013). Sea surface salinity observations from space with the SMOS satellite: A new means to monitor the marine branch of the water cycle. *Surveys in Geophysics*, *35*(3), 681–722. https://doi.org/10.1007/s10712-013-9244-0

Reynolds, D., Smith, T., Liu, C., Chelton, D., Casey, K., & Schlax, M. (2007). Daily high-resolution blended analyses for sea surface temperature. *Journal of Climate*, *20*(22), 5473–5496. https://doi.org/10.1175/2007JCL1824.1

Roemmich, D., & Owens, W. B. (2000). The ARGO project: Global ocean observations for understanding and prediction of climate variability. *Oceanography*, *13*(2), 45–50. https://doi.org/10.5670/oceanog.2000.33

Rudnick, D., Gopalakrishnan, G., & Cornuelle, B. (2015). Cyclonic eddies in the Gulf of Mexico by underwater gliders and simulations by numerical model. *Journal of Physical Oceanography*, *45*(1), 313–326. https://doi.org/10.1175/JPO-D-14-0138.1

Sena Martins, M., Serra, N., & Stammer, D. (2015). Spatial and temporal scales of sea surface salinity variability in the Atlantic Ocean. *Journal of Geophysical Research: Oceans*, *120*, 4306–4323. https://doi.org/10.1002/2014JC010649

Stammer, D. (1997). Global characteristics of ocean variability estimated from regional TOPEX/Poseidon altimeter measurements. *Journal of Physical Oceanography*, *27*(8), 1743–1769. https://doi.org/10.1175/1520-0485(1997)027<1743:GCOOVE>2.0.CO;2

Stumpf, H. G., & Legeckis, R. V. (1977). Satellite observations of mesoscale eddy dynamics in the eastern tropical Pacific Ocean. *Journal of Physical Oceanography*, *7*(5), 648–658. https://doi.org/10.1175/1520-0485(1977)007<0648:SOOMED>2.0.CO;2

Tang, W., Fore, A., Yueh, S., Lee, T., Hayashi, A., Sanchez-Franks, A., et al. (2017). Validating SMAP SSS with in-situ measurements. *Remote Sensing of Environment*, *200*, 326–340. https://doi.org/10.1016/j.rse.2017.08.021

Tchilibou, M., Delcroix, T., Alory, G., Arnault, S., & Reverdin, G. (2015). Variations of the tropical Atlantic and Pacific SSS minimum zones and their relations to the ITCZ and SPCZ rain bands (1979–2009). *Journal of Geophysical Research: Oceans*, *120*, 5090–5100. https://doi.org/10.1002/2015JC010836

Tréguier, A. M., Deshayes, J., Lique, C., Dussin, R., & Molines, J. M. (2012). Eddy contributions to the meridional transport of salt in the North Atlantic. *Journal of Geophysical Research*, *117*, C05010. https://doi.org/10.1029/2012JC007927

Ubelmann, C., & Fu, L.-L. (2011). Vorticity structures in the tropical Pacific from a numerical simulation. *Journal of Physical Oceanography*, *41*(8), 1455–1464. https://doi.org/10.1175/2011JPO4507.1

United Nations Educational, Scientific and Cultural Organization (1985). The international system of units (SI) in oceanography, UNESCO Technical papers, N°45, IAPSO Sci. N°32, Paris, France.

Villas Bôas, A. B., Sato, O. T., Chaigneau, A., & Castelão, G. P. (2015). The signature of mesoscale eddies on the air-sea turbulent heat fluxes in the South Atlantic Ocean. *Geophysical Research Letters*, *42*, 1856–1862. https://doi.org/10.1002/2015GL063105

Vinogradova, N. T., & Ponte, R. M. (2013). Small-scale variability in sea surface salinity and implications for satellite-derived measurement. *Journal of Atmospheric and Oceanic Technology*, *30*(11), 2689–2694. https://doi.org/10.1175/JTECH-D-13-00110.1

Willet, C. S., Leben, R. R., & Lavin, M. F. (2006). Eddies and tropical instability waves in the eastern tropical Pacific: A review. *Progress in Oceanography*, *69*(2-4), 218–238. https://doi.org/10.1016/pocean.2006.03.010.!

Wunsch, C. (1999). Where do ocean eddy heat fluxes matter? *Journal of Geophysical Research*, *104*(C6), 13,235–13,249. https://doi.org/10.1029/1999JC900062

Yin, X., Boutin, J., Reverdin, G., Lee, T., Arnault, S., & Martin, N. (2014). SMOS sea surface salinity signals of tropical instability waves. *Journal of Geophysical Research: Oceans*, *119*, 7811–7826. https://doi.org/10.1002/2014.JC009960